academicJournals

Vol. 9(2), pp. 14-22, August 2017
DOI: 10.5897/JETR2017.0622
Article Number: 4EA61AE65842
ISSN 2006-9790

http://www.academicjournals.org/JETR

Journal of Engineering and Technology Research

Full Length Research

Determination of dispersivity in the subsurface foreshores of River Mersey Outer Estuary

Okuroghoboye Diepreye Itugha[1] and Emmanuel Munakurogha Adigio[2*]

[1]Civil and Electrical/Electronic Engineering Department, Faculty of Engineering, Federal University Otuoke, Bayelsa State, Nigeria.
[2]Mechanical/Marine Engineering Department, Faculty of Engineering, Niger Delta University, Wilberforce Island, Bayelsa State, Nigeria.

Received 25 June, 2017; Accepted 27 July, 2017

This paper determines contaminant dispersivity in the coastal sand of River Mersey Outer Estuary using results of field measurement from dye solute injection. Dispersivity is an alternative parameter for describing the characteristic behaviour of porous media. In this case, 3-D plumes in 2-D Photo-images were taken from multiple injection zones across the foreshore. The colour images were calibrated, standardized and the optical intensity converted into concentration maps. Apparent dispersivity of the subsurface foreshore was graphically determined from spatial covariance tensors. The variances were obtained by subtracting the products of the zeroth moments and square of the mean location of mass centers from the second order moments, and results were divided by the zeroth moment. The variance tensors ($\sigma_{x'x'}^2$, and $\sigma_{y'y'}^2$) were plotted against their respective travel distance intervals. The result predicts linear increase of the variance of spread distance, enhancing estimate of dispersivity using the best fit relations $\sigma_{y'y'}{}^2 = 0.1464\bar{y}' - 0.00395$ and $\sigma_{x'x'}{}^2 = 0.01514\bar{x}' - 0.000152$ for the x-x and y-y planes. The dispersivity coefficient varied with increase in travel distance. It quantifies the rate of spreading of the mean concentration of the tracer front which shows dependence on the distance traveled by the front. The effect on the mean concentration at the injection point is therefore described by the area of the effective dispersivity coefficient controls.

Key words: Sand aquifers, porous media, injectate, vadose zone, ground water, transport of pollutant, contaminant transport.

INTRODUCTION

The subject of contamination, movement and transport of dilute substances in coastal subsurface foreshores still remain a challenging field of study in agriculture, engineering and hydrological sciences (Fetter, 1999; Domenico and Schwartz, 1998). It is wide in scope and the parameters controlling the random molecular activity

*Corresponding author. E-mail: emadigio@yahoo.com.

Figure 1. Area map showing injection zones and positions at outer RME with overview map [Balloon– injection zone; Circle– injection point; Line– area covered during experiments].

associated with fate and transport may not be easily quantified or accurately predicted due to the complexity of hydrological processes (Wexler, 1992; Zhang et al., 2002).

However, the movement and transport of dissolved pollutants in the subsurface have been researched for several decades both with analytical and numerical methods (Fetter, 1999; Diaw et al., 2001). These studies have also contributed to the role of tides in better understanding of the transport and migration of contaminant plumes in porous media, data quantification methods, and the use of analytical and numerical techniques (Lanyon et al., 1982; Chan and Mohsen, 1992; Farrell, 1994). Most of these studies actually dealt with contaminant transport in groundwater aquifers which differs as compared to the movement of pollutant plumes.

This work therefore, shows detail of the movement of injectate chemical driven by coastal tides in the vadose zone. The paper describes in detail, the measured full 2D contaminant plumes and the innovative technique used to convert the colour map images to concentration profiles. Also, dispersion coefficient estimates have been applied to describe the movement of the plumes relative to distances travelled in the relatively uniform beach sand aquifer. This is one of the few studies that focused on the contaminant transport and fate problems in subsurface sediments, hence an important contribution to coastal environment field data. It also relates to methods and choices available to hydrogeologic mapping of vadose zone water dynamics, landfill and industrial waste disposal site studies in coastal sediments. Figure 1 shows the location of the study area and injection point map of data collection zones at the River Mersey Estuary (RME).

Processing and calibration of digital image data

The spatial distribution of the images was transformed to identify parameters governing physical phenomena in the porous subsurface. The use of conservative dyes is prevalent in literature to enable qualitative and quantitative data calibration, especially for the purpose of visualizing the mixing patterns of contaminants in space and time. The conservative dye that is transmitted into the study field serves as optical tracer contaminant

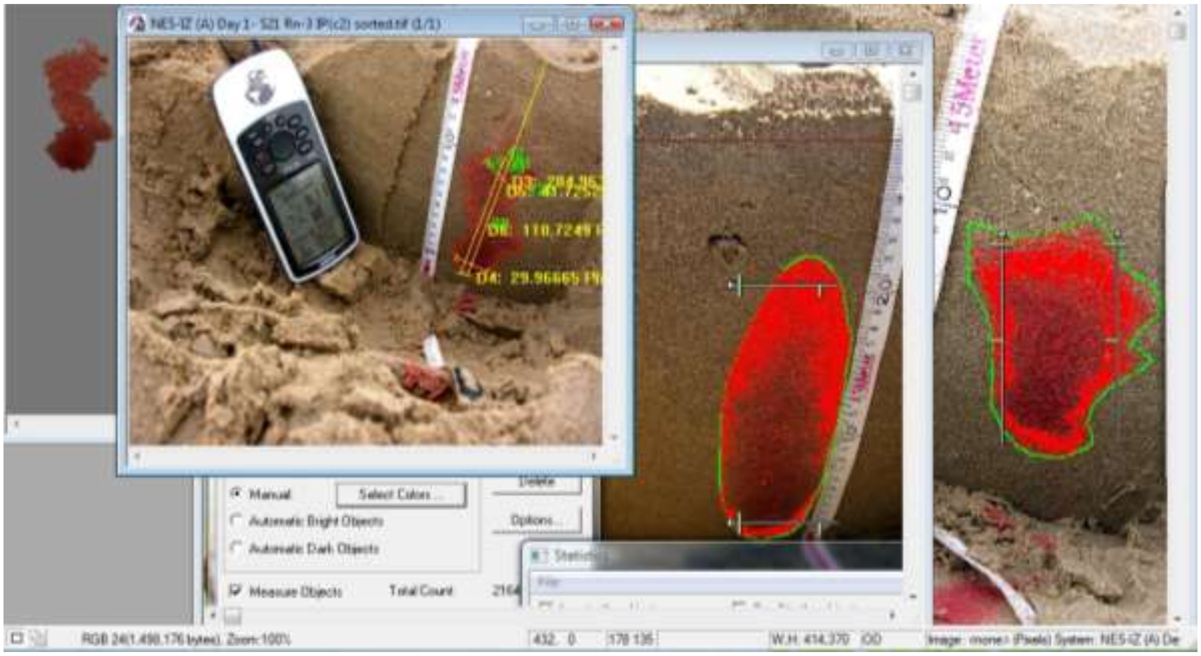

Figure 2. Sampled spatial segmentation and calibration of observed injectate plume geometries.

(Schincariol et al., 1993; Swartz and Schwartz, 1998; Rahman et al., 2005; McNeil et al., 2006).

Plume data geometry and processing

The data sampling sites in the field as shown in Figure 1 were grouped into three: (1) Winter data at OES-IZ(A), (2) Summer data at (i) OES-IZ(A) and (ii) OES-IZ(B)/NES-IZ(A), and (3) Summer data at OES-IZ(C)/NES-IZ(B) for convenience due to similarities observed in the dimensions and shapes of the plumes. Processed data was therefore analyzed relative to the aforementioned zones which may differ relatively in loading (compaction) or bed material type affecting nature of flow. All field data derived in the experiments were under natural oscillatory (tidal) unsaturation-saturation conditions.

The plume-pool in the flow direction between the surface of sand and the groundwater table aligns with the vertical y-axis = y' (longitudinal length) while flows parallel to the onshore-offshore oscillatory displacement is denoted as the horizontal x-axis = x' (transverse or perpendicular length). These concepts corresponds to the observed patterns of spread in the plumes whose average vertical distances were found relatively higher as compared to the width lengths in the OES-IZ(A) and OES-IZ(B)/NES-IZ(A) zones. However, in the first and third groups, that is winter [OES-IZ(A)] and summer [OES-IZ(C)/NES-IZ(B)] cases respectively, the horizontal size was larger hence the x-axis will be referred to as longitudinal.

The average size of the plumes (width) = $\overline{x}'$ and vertical length = $\overline{y}'$ relative to the depth of injection below the surface of the beach-sand were determined from the measured data. The mean diameter of the plume, and radius-ratios, etc. were also measured using the IPP caliper submenu along the major and minor axes for the vertical and width cross-sectional lengths, respectively. The average length of diameters was measured at 2° intervals through the plumes' centroids. The radius-ratio was measured using the ratio between the maximum radius of the plume and its minimum radius. Measurements were taken from the sand-surface in the direction of the water table.

The shapes of the plumes observed were mostly in conic and elliptic geometries (Figure 2). Although all images acquired from field were visually scaled (VST), spatial variation records of colour intensity and concentration was not readily measured *in situ*. Instead, photographic (digital) images of the chemical plumes taken with 8.0 effective megapixels Nikon E8800 Coolpix camera were extracted and processed. This procedure alienates the consequences of burying measuring devices for monitoring distribution of the chemical *in situ*.

According to Robbins (1989), solute monitoring devices are invasive, and could pose a problem to the effective flow stream of the solute in the subsurface natural environment. Hence, achieving quantitative concentration profiles in such environments may not be easily possible (Precht and Huettel, 2004). Non-invasive techniques require image processing tools, thus, Pro Plus (IPP) and MATLAB software programs were used. The IPP enables

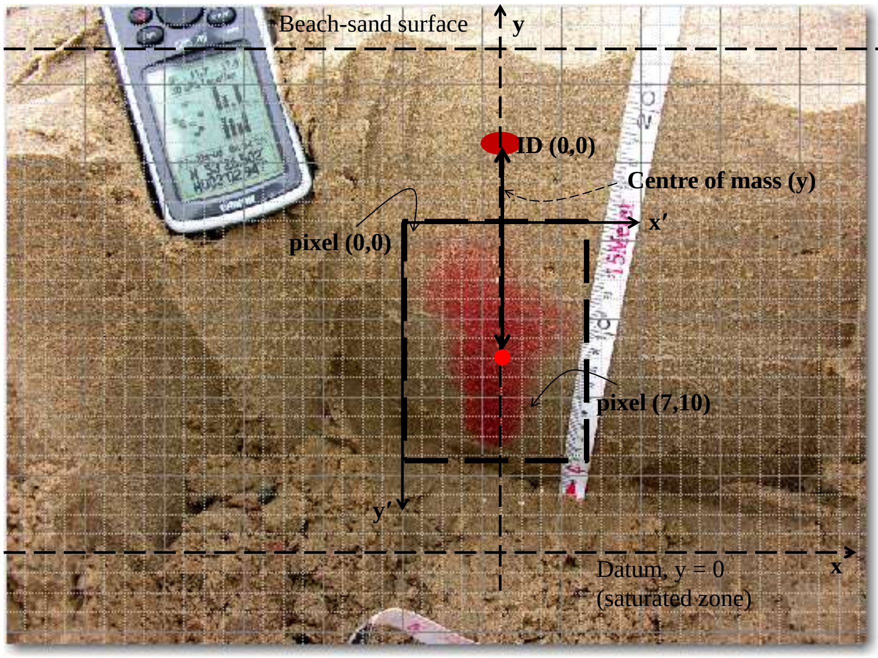

Figure 3. Pixel bitmap schematic (exaggerated) of digitization process for the injectate plume above GWT.

2D and 3D fluorescence imaging, filtering, spatial calibration, measurement and colour segmentation analyses. The processing operation involved enhancement of the digital photo-images, defining the area of interest (AOI) of the plume image, and then measuring the center of mass, area, tilted angle, lengths, etc. using the count/size submenu.

Image processing and digitization

The basis of digitizing and processing the photo-image is to be able to quantize the spatial distribution of the injectate concentration. That is, the conversion of the injectate plumes into concentration distribution maps using computer imaging techniques to manipulate 2-D plume-image data to digital formats (Harrison, 1990; Russ, 1992). The digital format expresses the image into horizontal grid in terms of an array, representing the colour intensity or the brightness by pixel values in the range of less than or equal to 1/300th pixels per inch (PPI). The pixel bitmap is expressed in width-size or rows (x) and vertical length-size or columns (y) numbers. The segmented AOI is defined using the positions (x_i',y_i') in the direction of x and y (Figure 3). The process samples individual pixels in the image in the range of 0 to 255, corresponding to the variation of color intensity from the darkest to the brightest. Some of the attributes of the IPP technique may consist of converting color to grey-scale, removal of noise and reduction in image data volume.

To enable information of the concentration, however, a quantitative description of color intensity-optical density intensity relationship was exacted. This is because optical density and light transmittance are related indirectly through the pixel range defined in the photographic negatives such that smaller optical density values are associated with brighter negatives. In the experiments, the solute was injected into the subsurface over several hours before tidal-invasion producing just one color (300 x 300 PPI) for digitization as grey-scale images. The pixel position (0,0) is therefore relative to the injection depth (ID) position (0,0) where the seawater joins the injectate (Figure 3). The digital image strips were optically processed using the unit specifier for 1000 pixels per meter scale (corresponding to about 0.032 m^2 photo-image). x_i**'** is the caliper diameter along the minor axis of the plume and y_i', the length along the major axis (i=0,1,2…) within the AOI.

Image data calibration

In the image data, each of the photographic colour images represents a variation of three primary colour components: red, green and blue (RGB) or known as image true colour. The IPP identifies each pixel of RGB image as consisting of equal-bit value and supports up to 48-bit colour images. In this study however, the relation between the color intensity of the images and color concentration of the solute chemical was determined by the method of calibration and setting thresholds (0 or 1) to each color pixels.

Firstly, the spatial distribution of color intensities was standardized to optical density intensity data and converted to concentration profiles using a least square relationship. Some researchers (Schincariol et al., 1993; McNeil et al., 2006) emphasized the standardization of image colour intensities to optical density (ρ_{opt}) levels. The intensity scales of image plumes in the process was calibrated and expressed as standard optical density data. The conversion to optical density was done through the 'measure' submenu by calling the intensity command after successful spatial calibration. The command activates the intensity calibration window and the standard optical density option was checked in favour of the gray scale. The emergent exponential curve interprets the optical density scale as inversely related to the optical density data $\left[\rho_{opt} = \log_{10}(m/I)\right]$, where ρ_{opt} = optical density intensity and 'm' imply constant of proportionality. The ratio of optical density/intensity shows that larger intensities would mean lesser optical density values. The standard deviations of the colour patches were evaluated in 2-D space with time across the entire cross-section of the segmented plume:

$$\sigma_x(t) = \left(N^{-1}\sum\left(x - \bar{x}_c(t)\right)^2 . f(x,y,t)\right)^{0.5} \text{ and}$$

$$\sigma_y(t) = \left(N^{-1}\sum\left(y - \bar{y}_c(t)\right)^2 . f(x,y,t)\right)^{0.5}$$

Where $\bar{x}_c(t)$ and $\bar{y}_c(t)$ represent the average spatial increments of the plume cross-sections.

Quantification of plume images

To quantify the geometric profiles of the image plumes, preliminary tests were conducted in the laboratory with dried samples of the field sediments. The method involved construction of rectangular boxes with volumetric dimension of 9.2 × 7.8 × 2.0 cm^3. The depth of field materials (completely dry sand) introduced was approximately 1.2 cm, such that the volume of sand introduced into the box(es) on each test occasion was 9.2 × 7.8 × 1.2 cm^3. Initially, 10 ml of undiluted injectate solute was introduced and allowed to be absorbed, and then photographed perpendicularly above the cross-section of the box. The solute sample with concentration of 43 mg/l was then diluted using calculated amounts of water (0.001 to 0.0099 l) varying from 0 to 0.043 mg/l. The Nikon camera recorded the images in jpg format which were converted to the lossless tiff file type for the image analysis.

The intensity of the black and incident or background levels was first established as 1 and 115, respectively, which were entered in the optical density calibration box. The density-distance plots were obtained through the line profile command provided by the IPP, including the statistical submenu. The statistical data was exported to Microsoft Excel for further processing, while the plots were saved into image tiff files using the IPP screen capture utility.

MATHEMATICAL BACKGROUND

Using the expression for the velocity and apparent (effective) dispersion coefficient in the x-direction where they are expressed as effective Langrangian characteristic properties in the form:

$$v_x = \frac{d\left(M_{100}/M_{000}\right)}{dt} \qquad (1)$$

and

$$D_{x'x'} = \frac{d}{dt}\left(\frac{M_{200}}{M_{000}} - \left(\frac{M_{100}}{M_{000}}\right)^2\right) \qquad (2)$$

The scale dependence of dispersivity was estimated by the second moment of the concentration distribution over known intervals resulting from the sampling sessions. The apparent dispersion coefficient is proportional to the time rate of change of the spatial second moment of the concentration distribution with the first moment (Equation 2). The sum of the product of dispersivity and linear pore water velocity, and molecular diffusion D_e generally describes the effective hydrodynamic coefficient of dispersion expressed here as:

$$D_h = \alpha v + D_e \qquad (3)$$

Where

$$\alpha_{x'x'} = \frac{d}{dx}\left(\frac{M_{200}}{M_{000}} - \left(\frac{M_{100}}{M_{000}}\right)^2\right) \qquad (4)$$

Apparent dispersivities were also estimated graphically by plotting the variance tensors against time or displacement distance, determining the linear best fit and using the expression $\alpha_{x'x'}$ = 0.5 (variance/travel distance) or:

$$\alpha_{x'x'} = 0.5 \times \text{Slope} \qquad (5)$$

The apparent (effective) dispersivity (Equation 5) is proportional to the rate of change of the spatial second moment of the concentration distribution with the first moment.

However, for the individual calibration of the transverse and longitudinal dispersion of the plumes, the Gaussian Operator in Matlab $C(x) = ae^{\left[-((x-b)/\sigma)^2\right]}$ was applied where $D = \sigma^2/4t$ = dispersion, σ = peak plume size or mixing length/width, b = peak location of center of plume and $a = \left(\sqrt{4\pi Dt}\right)^{-1}$ = peak amplitude.

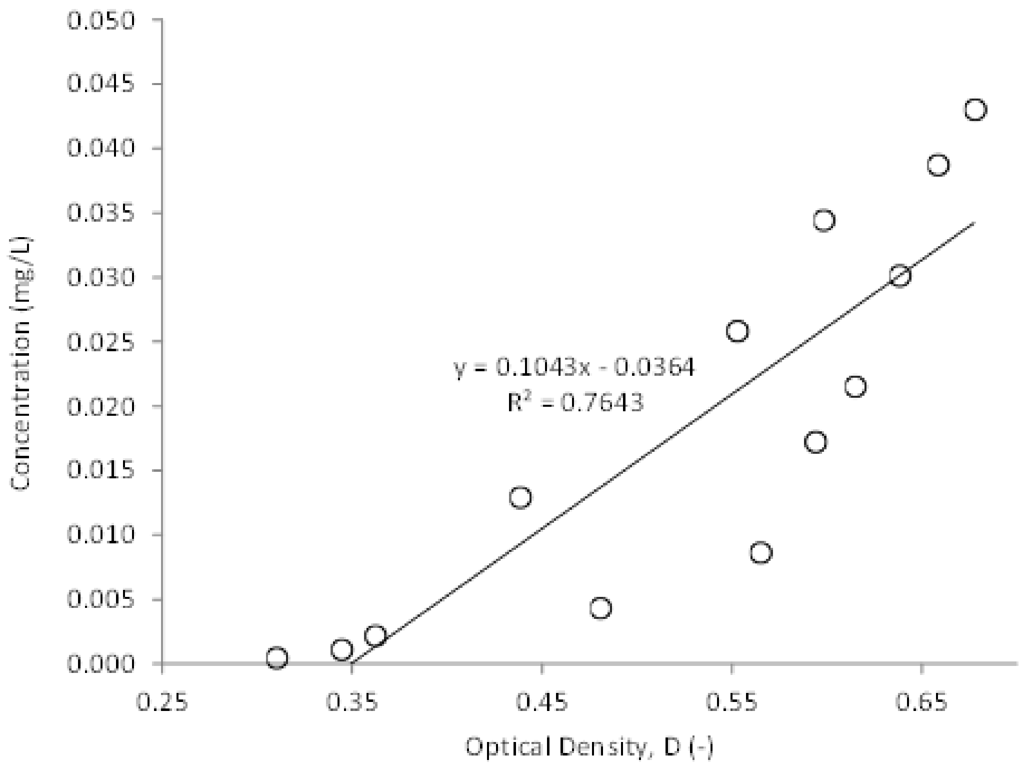

Figure 4. Curve of injectate concentration (mg/L) and standardized optical density intensity.

RESULTS AND DISCUSSION

Figure 4 presents the least square fit relative to the nonlinear form $C_r = m\rho_{opt}{}^{a}$ when the intensity data was standardized to optical density and plotted against concentration profiles. The value '*a*' refers to indicial power showing nonlinearity in the relation. The concentration data of the injectate images here was obtained using the nonlinear indicial power relation:

$$C = 0.3509 * \rho_{opt}{}^{5.3238} \tag{7}$$

The linear fit in the calibration estimated the relation to C = 0.1043 ρ_{opt} - 0.0364 with the *R*-squared value of 0.7643, while the nonlinear relative concentration case is shown in Figure 5. The nonlinear curve relation $C = 0.3509 * \rho_{opt}{}^{5.3238}$ was also applied with the *R*-squared value of 0.8952 in Equation 1. Some researchers (Zhang et al., 2002; Huang et al., 2002) did similar work applying their results from the calibration to convert observed photo images to solute concentration contours.

Details of plume intervals including the radius-ratios covering the 5-days duration of experimentation in the field for all the zones were established. The radius-ratios, which accounted for the effective growth in the spreading of the plumes, were plotted against the center of plumes for each zone (Figure 6). Sharp contrasts of increasing radius-ratio were observed for the summer [OES-IZ(C)/NES-IZ (B)] experiments which lasted for about a day. Also, in the summer [OES-IZ (B)/NES-IZ (A)] zones, the radius-ratios varied sharply with the location of mass centers as compared to the data of summer [OES-IZ (A)], where in both cases, the tracer tests were sustained for a period of one to five days. The sharp increases in the trends reflected higher plume-pool spreading in these zones.

The wide range of scatter in the data points is attributable to the widely varying sampling points across the study field. However, it can be concluded that the radius-ratios increases linearly with the movement or spreading of the injectate chemical within the boundaries of the vadose zone. The variances were obtained by subtracting the products of the zeroth moments and square of the mean location of mass centers from the second order moments, and the results were divided by the zeroth moment. The values obtained were slightly high but are consistently in the same order of magnitude values obtained by Garabedian et al. (1991) from tracer tests in Cape Cod over a depth of 1.0 m. This is understandable considering the depth and medium of investigation in this study, which is the vadose zone.

The range of values predicted for the winter [OEIS-IZ

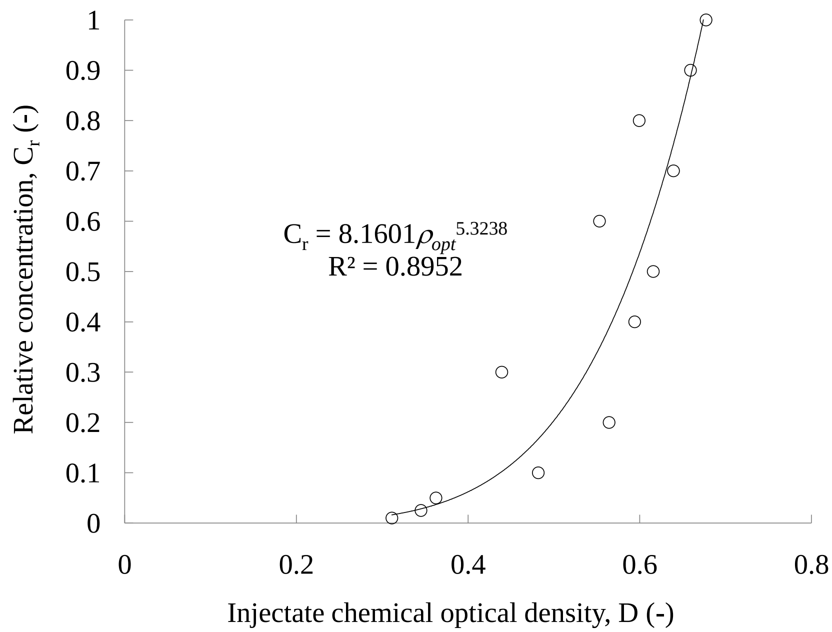

Figure 5. Curve of relative injectate concentration and standardized optical density intensity.

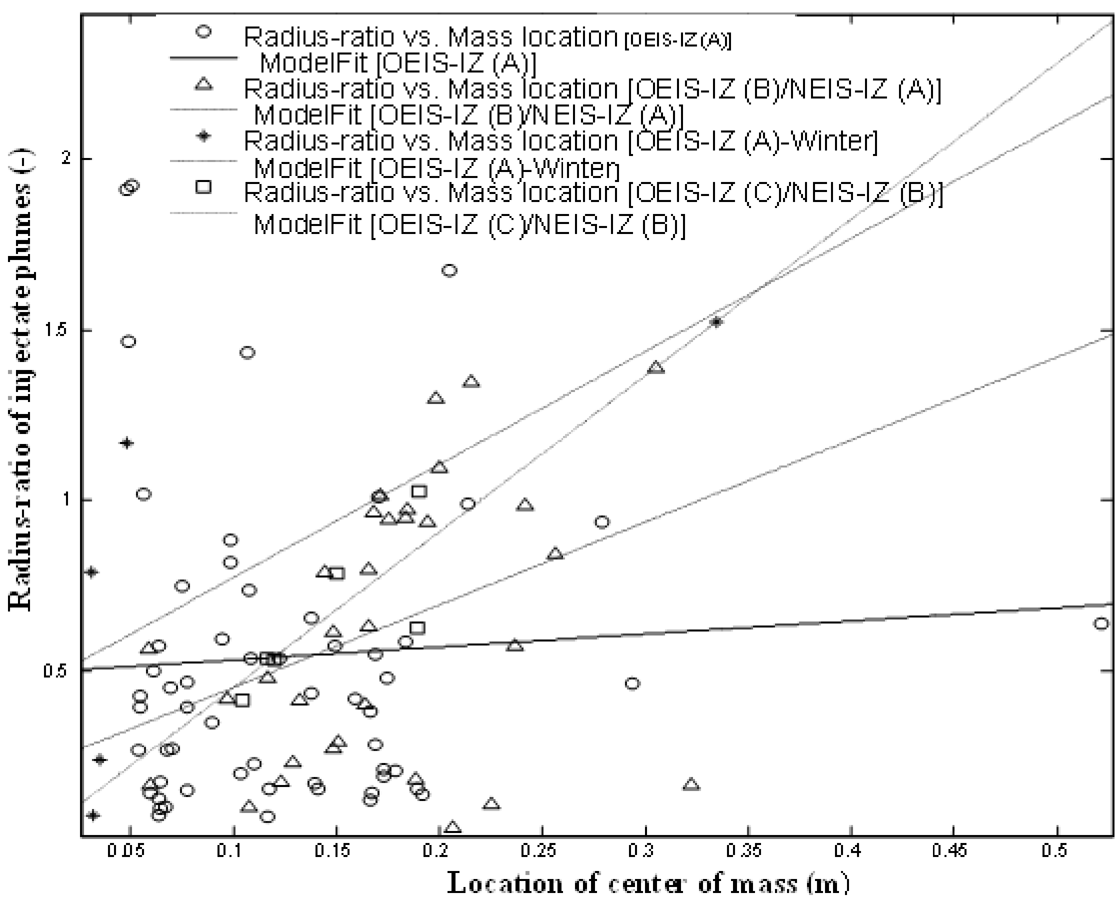

Figure 6. Mean radius-ratio and location of center of plume relationship from days-1 to 5. The fitted linear displacement trends relating to the zones during the experiments are shown in the legend.

(A)] represent data obtained for one day hence is comparable to the summer [OES-IZ (C)/NES-IZ (B)] data alone in this case. The growth in the plumes was faster in the winter with a magnitude of 0.01341 m/h within 95% confidence bounds (0.01341 and 0.01341 m/h), which is about twice those derived from the summer combination OES-IZ (C)/NES-IZ (B) for the same duration of time.

The velocities show that the surficial plane of the sand is likely the most affected by hydrodynamic events, implying that pressure penetration into deeper horizons in the vadose may weaken over time with increasing depth, which is consistent with findings in literature. The longitudinal and transverse hydrodynamic dispersion coefficients were simultaneously evaluated using concentration distribution curves from tracer tests observed in the field. Whole 2D plumes, implying the transverse and longitudinal cross-sections, were optimized to give full description of observed movement in the subsurface.

The dispersion coefficient increases with increasing changes observed in the movement of the center of plumes, which is interesting in-spite of the relatively uniform beach-sand. This is because in isotropic mediums, dispersion coefficients are usually assumed constant and the differences in concentration structures become less significant. The data shows that the gradients in the winter [OEIS-IZ (A)] and summer [[OEIS-IZ (B)/NEIS-IZ (A)] and [OEIS-IZ (C)/NEIS-IZ (B)]] zones are relatively similar or constant, implying about four (4) times higher mixing rates as compared to the summer [OEIS-IZ (A)] zone. The influence on the spread could be related to the increasing trends in the observed injectate pool cross-sectional area or radius-ratio with time.

The comparison showed in these experiments that the virtual dispersion coefficient asymptotically approached a steady state at some certain time and space and then tends to decrease.

Conclusion

A new tool, the IPP, in addition to MATLAB scripts have been successfully applied to process 2-D colour images of injectate chemical plumes recovered in the RME subsurface foreshores, as required in non-invasive techniques (Robbins 1989). Calibrated colour intensities of the plumes were standardized to optical density intensities for conversion to concentration profiles. Concentration data of the injectate images was obtained using a power law equation derived from calibration data. All the images measured are full 2D color contaminant (conservative injectate) plumes which were converted to concentration maps. Descriptions of data for all experimentation zones with 95% confidence intervals were established.

Virtual/effective dispersion coefficient was evaluated using calibration techniques and through determination of slopes. The dispersion coefficients varied with increase in travel distance in-spite of the relatively uniform sand grains of the beach. The resulting patterns are in agreement with findings in literature which assume both longitudinal and transverse dispersion coefficient as linear functions of growth in the injectate pool from the point of injection. The advective mean velocity was estimated using first order moments to account for the migration of the injectate chemical at average pore-water velocity, describing the natural consequence of heterogeneity and dispersion. The gradients obtained show that mixing rates were about 4 times higher in the winter [OEIS-IZ (A)] and summer [[OEIS-IZ (B)/NEIS-IZ (A)] and [OEIS-IZ (C)/NEIS-IZ (B)]] zones as compared to the summer [OEIS-IZ (A)] zone. It is thought that this condition affects the behaviour of movement in the summer [OEIS-IZ (A)] zone in particular, articulates the effective dispersivity characteristics of the porous medium in the vicinity of the water table due to the subsidence factor. It was also found that D_h increases linearly with increasing velocity with relatively constant slopes, indicating that the mixing lengths are almost constant across the zones investigated.

CONFLICT OF INTERESTS

The authors have not declared any conflict of interests.

REFERENCES

Chan SY, Mohson MFN (1992). Simulation of tidal effects on contaminant transport in porous media. Ground Water 30(1):78-86.

Diaw EB, Lehmann, Ackerer FPH (2001). One-dimensional simulation of solute transfer in saturated–unsaturated porous media using the discontinuous finite elements method. J. Contam. Hydrol. 51(3-4):197-213.

Domenico PA, Schwarz FW (1998). Physical and Chemical Hydrogeology. John Wiley & Sons, Inc.. ISBN 0-471-59762-7.

Farrell ER (1994). Analysis of groundwater flow through leaky marine retaining structures. Geotechnique 44(2):255-263.

Fetter CW (1999). Contaminant Hydrogeology, Second Edition, Prentice Hall Upper Saddle River, NJ 07458.

Garabedian SP, LeBlanc DR, Gelhar LW, Cella, MA (1991). Large Scale Natural Gradient Tracer Test in Sand and Gravel, Cape Cod, Massachusetts, 2, Analysis of Spatial Moments for a non-reactive Tracer. Water Res. Res. 27(5):911-924.

Harrison BA (1990). Introduction to Image Processing. CSIRO Australia. P 256.

Huang WE, Colin CS, David NL, Steven FT, Adrian O (2002). Physical modelling of solute transport in porous media: evaluation of an imaging technique using UV excited fluorescent dye. Water Res. 36:1843-1853.

Lanyon JA, Eliot IG, Clarke DJ (1982). Groundwater–level variation during semidiurnal spring tidal cycles on a sandy beach. Austr. J. Marine Freshwater Res. 33:377-400.

McNeil JD, Oldenborger GA, Schincariol RA (2006). Quantitative imaging of contaminant distributions in heterogeneous porous media laboratory experiments. J. Contam. Hydrol. 84:36-54.

Precht E, Huettel M (2004). Rapid wave-driven advective pore water exchange in a permeable coastal sediment. J. Sea Res. 51:93-107.

Rahman A, Jose S, Nowak W, Cirpka O (2005). Experiments on vertical transverse mixing in a large-scale heterogeneous model aquifer. J.

Contam. Hydrol. 80:130-148.
Robbins GA (1989). Methods for determining transverse dispersion coefficients of porous-media in laboratory column experiments. Water Resour. Res. 25:1249-1358.
Russ JC (1992). The image processing handbook, CRC Press Inc. P 445.
Schincariol RA, Herderick EE, Schwartz FW (1993). On the application of image analysis to determine concentration distributions in lab excepts. J. Contam. Hydrol. 12:197-215
Swartz CH, Schwartz FW (1998). An experimental study of mixing and instability development in variable-density systems. J. Contam. Hydrol. 34:169-189.
Wexler EJ (1992). Analytical solutions for one-, two-, and three dimensional solute transport in groundwater systems with uniform flow. U.S. Geological Survey, Techniques of Water-Resources Investigations, Book 3, Chapter B7.
Zhang Q, Volker RE, Lockington DA (2002). Experimental investigation of contaminant transport in coastal groundwater. Adv. Environ. Res. 6:229-237.